Available online at www.sciencedirect.com

SCIENCE DIRECT®

Tectonophysics 384 (2004) 149–174

TECTONOPHYSICS

www.elsevier.com/locate/tecto

Numerical studies on the failure process and associated microseismicity in rock under triaxial compression

H.Y. Liu[a,*], S.Q. Kou[a], P.-A. Lindqvist[a], C.A. Tang[b]

[a] *Department of Civil and Mining Engineering, Luleå University of Technology, SE-97187, Luleå, Sweden*
[b] *Center for Rock Instability and Seismicity Research, Northeastern University, 110006, Shenyang, China*

Received 6 June 2003; accepted 25 March 2004
Available online 14 May 2004

Abstract

In this paper, firstly the mesoscopic elemental mechanical model for elastic damage is developed and implemented into the rock and tool interaction code (R-T^{2D}). Then the failure processes of a heterogeneous rock specimen subjected to a wide variety of confining pressures (0–80 MPa) are numerically investigated using the R-T^{2D} code. According to the simulated results, on the one hand, the numerical simulation reproduced some of the well-known phenomena observed by previous researchers in triaxial tests. Under uniaxial compression, rock failure is caused by a combination of axial splitting and shearing. Dilatancy and a post-failure stage with a descending load bearing capacity are the prominent characteristics of the failure. As the confining pressure increases, the extension of the failed sites is suppressed, but the individual failure sites become dense and link with each other to form a shear fracture plane. Correspondingly, the peak strength, the residual strength and the shear fracture plane angle increase, but the brittleness decreases. When the confining pressure is high enough, the specimen behaves in a plastic manner and a narrow shear fracture plane leads to its failure. The prominent characteristics are volume condensation, ductile cataclastic failure, and a constant load bearing capacity with increasing strain. On the other hand, the numerical simulation revealed some new phenomena. The highest microseismicity events occur in the post-failure stage instead of the maximal stress, and most of the microseismicity energies are released in the failure localization process. As the confining pressure increases, the microseismicity events in the non-linear deformation stage increase dramatically and the ratio between the energies dissipated at the non-linear deformation stage and those dissipated in the whole loading process increases correspondingly. Therefore, it is concluded that the developed mesoscopic elemental mechanical model for elastic damage is able to reproduce accurately the failure characteristics in loading rock specimens under triaxial conditions, and the numerical modelling can furthermore obtain some new clarifications of the rock fracture process.

Keywords: Numerical simulation; Failure process; Microseismicity; Failure mechanism; Triaxial tests

1. Introduction

Detecting fracture nucleation and understanding the progressive process of faulting are important keys to earthquake prediction. The study of rock fracture under triaxial conditions captures the essential features. Laboratory experiments have traditionally been used as a

* Corresponding author. Tel.: +46-920-491440; fax: +46-920-491935.
E-mail address: Hong-Yuan.Liu@ce.luth.se (H.Y. Liu).

0040-1951/$ - see front matter © 2004 Elsevier B.V. All rights reserved.
doi:10.1016/j.tecto.2004.03.012

simple and effective way to investigate the progressive failure process and associated microseismicities in rock material under triaxial compression. In the recent past, advanced techniques, such as the optical microscope (Moore and Lockner, 1995), the scanning electron microscope (SEM, Tapponnier and Brace, 1976; Kranz, 1983; Shimada and Cho, 1990; Wu et al., 2000), elastic-wave propagation measurement (Ayling et al., 1995), acoustic emission (AE) detection (Lockner et al., 1992; Cox and Meredith, 1993) and the X-ray computerized tomography (CT) scanning system (Kawakata et al., 1999), have been applied to laboratory experiments by numerous researchers to monitor the progressive failure process and associated microseismicities. These advanced studies have enhanced our understanding of the progressive nature of failure and associated microseismicities within rock under compression. It is now recognized that the macroscopic faulting process in a brittle rock actually involves a multiplicity of microcracks, and its essential nature lies not only in the initiation and propagation of individual cracks, but also in the interaction and coalescence of the crack population. On the one hand, whilst physical descriptions of fracture phenomena encountered within stressed rock materials have been established by laboratory experiments and field observations, an accurate prediction of these phenomena remains one of the most difficult tasks in the study of rock mechanics (Fang and Harrison, 2002b). On the other hand, microscopic observations cannot be made non-destructively, elastic wave propagation and AE detection need to relate the changes in physical properties and AE events to cracking activities, and the X-ray CT scanning system is too complicated, time-consuming and expensive to use.

Fracture mechanics theory predicts fracture generation by relating the applied stresses to the propagation of a predefined crack (Whittaker et al., 1992), but the coalescence of cracks is difficult to describe using this theory, due to the constant and complicated changes to the boundary conditions that the dynamic microcracking events induce (Fang and Harrison, 2002b). Moreover, analytical models have to be simplified and sometimes this simplification ignores important factors influencing the material behaviour. For rock materials, heterogeneity is an example of such a factor. Due to heterogeneity, the fracture pattern in rock usually consists of a main crack with various branches, secondary cracks and microcracks (Liu, 2003).

With the rapid development of computing power, interactive computer graphics and topological data structure, numerical modelling has met with great success in predicting the fracture processes within a stressed rock material; see for example the studies of Tang (1997), Blair and Cook (1998), Tang et al. (2000), Fang and Harrison (2002b), Tang et al. (2002) and Liu (2003). Whether numerical techniques will generate realistic results or not depends on the incorporation of robust numerical methods that can allow the efficient resolution of multiple interacting cracks and rigorous fracture models that can reflect the material fabric characteristics. At present, the finite element method is the most mature numerical method. Recently, the damage mechanical model has become a powerful tool to model the non-linear behaviour induced in rock materials, which are subjected to a progressive microcracking process. Most of the damage mechanical models are based on homogenizing the rock body and finding its response by degrading the elasticity of the material (Lemaitre, 1992; Fanella and Krajcinovic, 1988; Lee and Ju, 1991; Hori and Morihiro, 1998).

In the present paper, in order to provide a powerful tool to understand the mechanisms that lead to macroscopic failure in heterogeneous rock material and, at the same time, refine the theories of damage utilized in continuum models, a mesoscopic elemental mechanical model for elastic damage is developed. The developed model is coupled into the rock and tool interaction code (R-T^{2D}) on the basis of the finite element method to perform research on the micro-mechanics of failure and associated microseismicity in a heterogeneous rock specimen under confining pressures of 0, 20, 40 and 80 MPa. According to the simulated results, the development of fracture from the mesoscopic elemental scale to the macroscopic scale, the brittle to semi-brittle and ductile transitions, the fracture patterns and the energy dissipation characteristics are discussed.

2. Mesoscopic elemental mechanical model for elastic damage

As mentioned in the Introduction, the damage mechanical model has become a powerful tool to

model the non-linear behaviour of rock materials which are subjected to a progressive microcracking process, by degrading the elasticity of the rock material. The mesoscopic elemental mechanical model for elastic damage, the subject of this paper, falls under this category of model. Here it is used to describe the mechanical behaviour of mesoscopic elements in a rock specimen due to the simplicity of its formulation, as well as its good performance from a numerical point of view. Rock is a heterogeneous material and the main reason for its failure is the process of initiation and propagation of microcracks, typically ranging from 0.01 to 1 mm in width (Cerrolaza and Garcia, 1997). This process leads to a concentration of these microcracks into a very narrow zone, causing a visible macrocrack or fissure wider than 1 mm (Cerrolaza and Garcia, 1997). Therefore, in the present paper rock fracture is analysed at the mesoscopic level. At the beginning, the element in the finite element method is considered to be isotropically elastic and its elastic properties can be defined by the Young's modulus and Poisson's ratio. The stress–strain curve of the element is considered linear elastic until the given damage threshold is attained, and is then followed by softening. For simplicity, an elastic damage model with a constant residual strength under uniaxial loading is used, as shown in Fig. 1. The maximum tensile stress criterion and the double elliptic strength criterion (Liu et al., 2002) are selected as two damage thresholds. In all cases the tensile stress criterion is preferable. It has been proved that the macroscopic mechanical response of rock at the macroscopic level can be simulated effectively by using this simple mesoscopic elemental mechanical model (Tang et al., 2000, 2002; Zhu, 2001; Liu, 2003).

The elastic damage constitutive relations for a mesoscopic element under uniaxial compressive stress and tensile stress are illustrated in Fig. 1. When the stress of the element satisfies the strength criterion, the element begins to fail. In elastic damage mechanics, the elastic modulus of material may degrade gradually as a damage progress. The elastic modulus of damaged material is defined as follows (Lemaitre, 1992):

$$E = (1 - D)E_0 \tag{1}$$

where D represents the damage variable. E and E_0 are the elastic modulus of the damaged and the undamaged material, respectively. It must be pointed out that in the present paper, the element and its damage are assumed to be isotropic. Therefore, E, E_0 and D are all scalar.

Following the regulations in rock mechanics, tensile stress and dilatant strain are referred to as negative, and compressive stress and contractional strain are referred to as positive throughout this paper. When

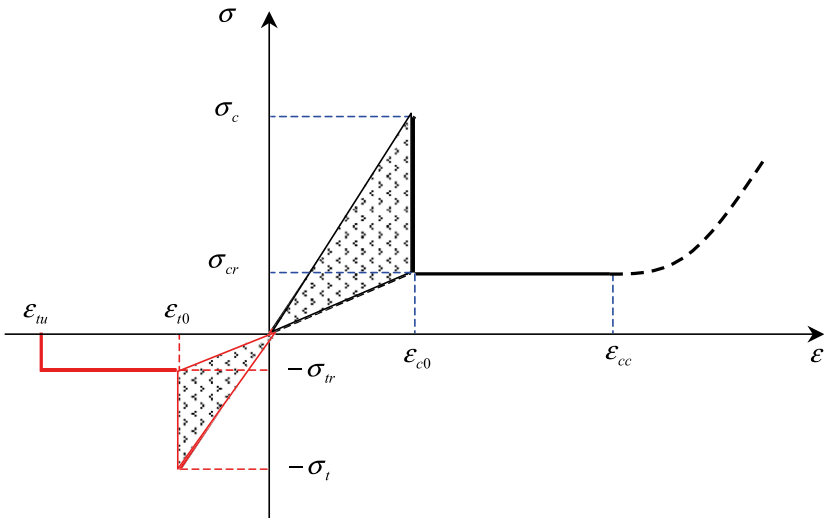

Fig. 1. Mesoscopic elemental constitutive relations under uniaxial compressive stress and tensile stress.

the mesoscopic element is under uniaxial tensile stress, the constitutive relation is that shown in Fig. 1 (the lower part of the figure), which is the elastic–brittle damage under tensile stress with a given specific residual strength. No initial damage is incorporated in this model, and at the beginning the stress–strain curve is linear elastic and no damage occurs, i.e. $D=0$. When the maximum tensile stress criterion is met, the damage of the element occurs. Therefore this kind of damage is also called tensile failure.

Under uniaxial tensile stress as described in Fig. 1, damage occurs when the tensile stress in an element reaches its tensile strength, σ_t, i.e.

$$\sigma_3 \leq -\sigma_t \tag{2}$$

The damage evolution of the mesoscopic element can be expressed as follows:

$$D=\begin{cases} 0 & \varepsilon > \varepsilon_{t0} \\ 1-\dfrac{\sigma_{tr}}{E_0\varepsilon} & \varepsilon_{t0} \geq \varepsilon > \varepsilon_{tu} \\ 1 & \varepsilon \leq \varepsilon_{tu} \end{cases} \tag{3}$$

where σ_{tr} is the residual tensile strength, which is defined as $\sigma_{tr}=\lambda\sigma_t=\lambda E_0\varepsilon_{t0}$. λ is the residual strength coefficient. ε_{t0} is the tensile strain at the elastic limit, which is the so-called tensile threshold strain. ε_{tu} is the ultimate tensile strain of the element, which indicates that the element would be completely damaged when the tensile strain of the element attains this ultimate tensile strain. The ultimate tensile strain is defined as $\varepsilon_{tu}=\eta\varepsilon_{t0}$, where η is called the ultimate tensile strain coefficient. In terms of the strains, the damage evolution equation of the mesoscopic element under uniaxial tensile loading can also be expressed as follows:

$$D=\begin{cases} 0 & \varepsilon > \varepsilon_{t0} \\ 1-\dfrac{\lambda\varepsilon_{t0}}{\varepsilon} & \varepsilon_{t0} \geq \varepsilon > \varepsilon_{tu} \\ 1 & \varepsilon \leq \varepsilon_{tu} \end{cases} \tag{4}$$

Moreover, it is assumed that the damage of a mesoscopic element in the multiaxial stress field is also isotropic. According to the method of extending the one-dimensional constitutive law under uniaxial-tensile to complex-tensile stress conditions, the above-described constitutive law for uniaxial tensile stress can be extended to use for three-dimensional stress states. Under multiaxial stress states the element is still damaged in the tensile mode when the combination of major tensile strains attains the above threshold strain ε_{t0}. The constitutive law of an element subjected to multiaxial stresses can be easily obtained by merely substituting the strain ε in Eq. (4) with an equivalent strain $\bar{\varepsilon}$. The equivalent strain $\bar{\varepsilon}$ is represented by using the following nonsymmetric criterion (Cerrolaza and Garcia, 1997):

$$\bar{\varepsilon}=\sqrt{\langle\varepsilon_1\rangle_-^2+\langle\varepsilon_2\rangle_-^2+\langle\varepsilon_3\rangle_-^2} \tag{5}$$

which in the case of plane strain becomes $\bar{\varepsilon}=\sqrt{\langle\varepsilon_1\rangle_-^2+\langle\varepsilon_3\rangle_-^2}$, where ε_i represents the principal strains and $\langle\varepsilon_i\rangle_-=[\varepsilon_i-abs(\varepsilon_i)]/2$. The criterion was first developed for concrete and it was adopted here for rock, since both materials are more resistant to damage in compression than in traction. Microscopic observations have shown that cracks always have an orientation mainly normal to the principal strain directions. This is why the criterion depends only on the negative strains (Cerrolaza and Garcia, 1997).

$$\langle\varepsilon_i\rangle_- = \varepsilon_i \quad \text{if } \varepsilon_i \leq 0, \text{ a case of tensile strain} \tag{6}$$

$$\langle\varepsilon_i\rangle_- = 0 \quad \text{if } \varepsilon_i > 0, \text{ a case of compressive strain} \tag{7}$$

It must be emphasized that when $D=1$, it is calculated from Eq. (1) that the damaged elastic modulus is zero, which would make the system of equations ill-conditioned. Therefore, in the model a relatively small number, i.e. 1.0×10^{-5}, is specified for the elastic modulus owing to this consideration.

To describe the mesoscopic elemental damage under a compressive or shear stress condition, we choose the double elliptic strength criterion (Liu et al., 2002) as the second damage criterion, shown in Fig. 2, i.e.

$$\begin{cases} a\sqrt{\sigma_g^2+4\tau_g^2}+b\sigma_g=c, \tau_g \geq k\sigma_g \\ a'\sqrt{\sigma_g^2+4\tau_g^2}+b'\sigma_g=c, \tau_g < k\sigma_g \end{cases} \tag{8}$$

where a, b, a', b' and c are constant parameters, which can be defined according to the stress conditions at the

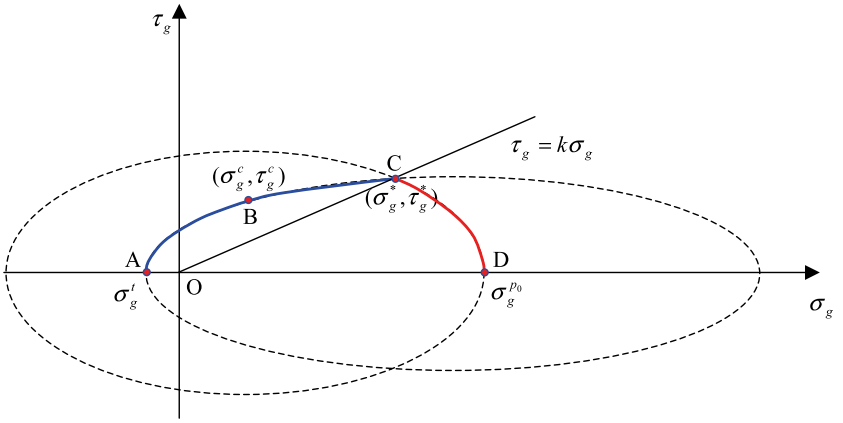

Fig. 2. Double elliptic strength criterion by generalized shear and normal stress representation.

triaxial tensile limiting stress state, i.e. Point A (σ_g^t, 0) in Fig. 2, at the uniaxial compressive limiting stress state, i.e. Point B (σ_g^c, τ_g^c) in Fig. 2, at the brittle to ductile failure transition limiting stress state, i.e. Point C (σ_g^*, τ_g^*) in Fig. 2, and at the hydrostatic pressure yield limiting stress state, i.e. Point D ($\sigma_g^{P_0}$, 0) in Fig. 2. $\sigma_g = \sigma_1 + \sigma_3$ and $\tau_g = \sigma_1 - \sigma_3$, where σ_1 and σ_3 are the major and minor principal stress, respectively; and σ_g and τ_g are the generalized normal and shear stress, respectively. $\sigma_g^t = -2\sigma_t$ is the generalized normal stress at the triaxial tensile limiting stress state, where σ_t is the uniaxial tensile strength. $\sigma_g^c = \sigma_c$ and $\tau_g^c = \sigma_c$ are the generalized normal and shear stress at the uniaxial compressive limiting stress state, where σ_c is the uniaxial compressive strength. σ_g^* and τ_g^* are the generalized normal and shear stress at the brittle to ductile failure transition limiting stress state. Hoek and Brown (1980) chose the relationship $\sigma_1 = 3.4\sigma_3$ ($\tau_g = k\sigma_g$, where $k = 6/11$, in a generalized shear and normal stress presentation) as the best approximation of the brittle–ductile transition. $\sigma_g^{P_0} = 2P_0$ is the generalized normal stress at the hydrostatic pressure yield limiting stress state, where P_0 is the hydrostatic pressure. The uniaxial tensile strength σ_t, the uniaxial compressive strength σ_c, and the hydrostatic pressure P_0 can be determined on the basis of laboratory test and the brittle to ductile failure transition point (σ_g^*, τ_g^*) can be obtained by solving the cross point between the Mohr–Coulomb strength envelope and the critical state line proposed by Hoek and Brown (1980). Therefore, the double elliptic strength criterion is feasible. As introduced in a previous paper (Liu et al., 2002), the brittle failure face of the double elliptic criterion will represent rock failure in the shear mode at a low confining pressure, just as the Mohr–Coulomb or Hoek–Brown strength criterion. The ductile failure face will represent rock failure in the ductile cataclastic mode at a high confining pressure. Compared with the Mohr–Coulomb strength criterion with a Roscoe cap, the major advantages of the double elliptic strength criterion is that it avoids the tip angle in the tension area in the Mohr–Coulomb strength criterion, and the failure criterion and yield cap model have the unified mathematical form, in which the ductile yield face is interrelated with the brittle failure face.

At a low confining pressure ($\tau_g \geq k\sigma_g$), on the basis of the uniaxial tensile strength σ_t and uniaxial compressive strength σ_c, the brittle failure conditions in the double elliptic strength criterion can be represented as follows (see Appendix A):

$$\frac{(2\gamma+1)\sqrt{\sigma_g^2 + 4\tau_g^2} + (2\gamma - \sqrt{5})\sigma_g}{2\gamma(1+\sqrt{5})} \geq \sigma_c \tag{9}$$

where $\gamma = \sigma_t/\sigma_c$ is the ratio between the uniaxial tensile strength and the uniaxial compressive strength.

When the stresses of the element satisfy the brittle failure conditions, shear damage is induced. A similar constitutive law is given in Fig. 1 (the upper part of the figure) when the element is under uniaxial compression and damage occurs in the shear mode according to the brittle failure condition of the double

elliptic strength criterion. The damage variable D can be described as follows:

$$D = \begin{cases} 0 & \varepsilon < \varepsilon_{c0} \\ 1 - \dfrac{\sigma_{cr}}{E_0 \varepsilon} & \varepsilon_{c0} \leq \varepsilon < \varepsilon_{cc} \end{cases} \tag{10}$$

where σ_{cr} is the residual compressive strength. It is assumed that $\sigma_{cr}/\sigma_c = \sigma_{tr}/\sigma_t = \lambda$ holds true when the mesocopic element is under uniaxial compression or tension. Similarly to the uniaxial tensile case, ε_{c0} is the compressive strain at the elastic limit, which is the so-called compressive threshold strain. ε_{cc} is the re-compaction compressive strain of the element, which indicates that the re-compaction behaviour occurs when the compressive strain of the element attains this re-compaction compressive strain. The re-compaction compressive strain is defined as $\varepsilon_{cc} = \xi \varepsilon_{c0}$, where ξ is called the re-compaction compressive strain coefficient.

When the element is under a multi-axial stress state and satisfies the brittle failure surface of the double elliptic strength criterion, shear damage occurs, and we must consider the effect of other principal stress in this model during the damage evolution process. When the brittle failure surface of the double elliptic strength criterion is met, the compressive threshold strain ε_{c0} can be calculated as follows (see Appendix A):

$$\begin{aligned} \varepsilon_{c0} &= \frac{1}{E_0}[\sigma_1 - v(\sigma_2 + \sigma_3)] \\ &= \frac{1}{E_0}\Bigg\{ -v(\sigma_2 + \sigma_3) + \frac{1}{2\gamma(4\gamma + 5 + \sqrt{5})} \\ &\quad \times \Big\{ 2\sigma_3[4\gamma^2 + (3 - \sqrt{5})\gamma + 2] \\ &\quad + \gamma\sigma_{cr}[-2(1 + \sqrt{5})\gamma + 5 + \sqrt{5}] \\ &\quad + sqrt\Big\{ 16\sigma_3^2[-4(1 + \sqrt{5})\gamma^3 - 4\sqrt{5}\gamma^2 \\ &\quad + (3 - \sqrt{5})\gamma + 1] + 8\gamma\sigma_3\sigma_{cr}[-8(1 + \sqrt{5})\gamma^3 \\ &\quad + 4(3 - \sqrt{5})\gamma^2 + 2(9 + \sqrt{5})\gamma + (5 + \sqrt{5})] \\ &\quad + 10(3 + \sqrt{5})\gamma^2\sigma_{cr}^2(4\gamma^2 + 4\gamma + 1)\Big\}\Big\}\Bigg\} \end{aligned} \tag{11}$$

In addition, it is assumed that the damage evolution is only related to the maximum compressive principal strain ε_1. Therefore, the maximum compressive principal strain ε_1 of the damaged element is used to substitute the uniaxial compressive strain ε in Eq. (10). Thus, the Eq. (10) can be extended to biaxial or triaxial stress states.

$$D = \begin{cases} 0 & \varepsilon_1 < \varepsilon_{c0} \\ 1 - \dfrac{\lambda \varepsilon_{c0}}{\varepsilon} & \varepsilon_{c0} \leq \varepsilon_1 < \varepsilon_{cc} \end{cases} \tag{12}$$

From the above derivation of the damage variable D (Eqs. (4) and (12)), which is generally called the damage evolution law in damage mechanics, as well as the previous Eq. (1), the damaged elastic modulus of the element at different stress or strain levels can be calculated. The unloaded element without failure keeps its original elastic modulus and strength. That is to say, the element without failure will unload elastically and no residual deformation is incorporated in the numerical model.

At a high confining pressure ($\tau_g < k\sigma_g$), no strength reduction is introduced. Therefore, when the ductile failure surface of the double elliptic strength criterion is met, the compressive threshold strain ε_{c0} is calculated in the same way as Eq. (11), except for substituting σ_{cr} with σ_c.

When the maximum compressive principal strain ε_1 of the element exceeds the re-compaction compressive strain ε_{cc}, i.e. $\varepsilon_1 \geq \varepsilon_{cc}$, re-compaction of the element occurs. In other words, the fractured elements can be re-compacted to form a new material with properties similar to those of intact elements depending on the lateral pressure when the compression strain of the element reaches a certain level. This phenomenon can be often observed either in percussive drilling, crushing or grinding of rocks, where the re-compacted fractured rock is usually stuck on the tool or equipment. Lindqvist (1982) has performed some experiments to validate the existence of the re-compaction behaviour. Moreover, the evidence for this kind of re-compaction behaviour can also be found independently in the work of Lai et al. (1980) and Lundqvist (1981). In this case, the elastic modulus of the element is gradually increased to resist the continuous compression.

Zhu (2001) and Tang et al. (2002) used this model to simulate the brittle failure of concrete and the permeability changes of rock masses, respectively, coupling the model with the Mohr–Coulomb strength criterion, in such a way that, when the Mohr–Coulomb strength criterion was satisfied, the compressive threshold strain ε_{c0} was calculated as follows:

$$\varepsilon_{c0} = \frac{1}{E_0}\left[-\nu(\sigma_2+\sigma_3)+\sigma_{cr}+\frac{1+\sin\phi}{1-\sin\phi}\sigma_3\right] \quad (13)$$

where ϕ is the internal friction angle. However, since the Mohr–Coulomb strength criterion is only valid for the brittle part of the rock failure envelope (Verhoef and Ockeloen, 1996; Zhao, 2000), it cannot describe the rock behaviour under high confining pressures. It should be noted that due to the lack of specific failure criteria for rock elements, the failure criteria developed based on the testing of laboratory scale rock specimens are used here for rock elements. On the basis of the argument developed by Fang and Harrison (2002a) that a rock element within a rock specimen can be considered as analogous to a rock specimen itself, the failure criteria for rock specimens may be applicable to rock elements.

How parameters such as the residual strength coefficient λ, the ultimate tensile strain coefficient η and the re-compaction compressive strain coefficient ξ affect the macroscopic behaviour of the constructed numerical model has been discussed in detail in previous papers/theses (Tang et al., 2000; Zhu, 2001; Liu, 2003). It has been proved that the effects of the constitutive parameters are minor, as long as the residual strength coefficient λ, the ultimate tensile strain coefficient η and the re-compaction compressive strain coefficient ξ are in the range $0<\lambda\leq 0.1$, $1.5\leq\eta\leq 5$ and $1.5\leq\xi\leq 5$, respectively. Calibration studies on some typical physical–mechanical and fracture mechanics experiments have been undertaken and proved that this model can effectively simulate the non-linearity of the stress–strain response, localization of deformation, strain softening, and crack initiation, propagation, interaction and coalescence in heterogeneous rock under a variety of quasi-static loadings (Liu, 2003).

Therefore, the simulation of failure initiation and fracture propagation in this investigation is the same as the method used in the smeared crack model, in that the crack is smeared over the whole element, which has the advantage of leaving the mesh topology untouched. No special singular element is adopted. When the stress state of an element meets the damage threshold, the element will be damaged in the tensile or shear mode. Only when the maximum tensile strain of the damaged element attains a given ultimate tensile strain, will the damaged element become totally cracked. One of the main features of this kind of model is that there is no need for a pre-fabricated notch to simulate the failure initiation and fracture propagation. Moreover, this model has obvious advantages compared with the model under the discrete crack framework, where usual formulations assume that a crack, once it opens, does not close; i.e. there is no consideration of a possible re-establishment of contact between the crack surfaces. However, the shortcoming of the mesoscopic elemental mechanical model for elastic damage is that it requires much more computer capacity for the same microstructural window of rock.

In a brittle or quasi-brittle material such as rock, acoustic emission (AE) is predominantly related to the release of elastic energy (Tang, 1997). Therefore, as an approximation, it is reasonable to assume that the AE counts are proportional to the number of damaged elements, and the strain energies released by damaged elements are all in the form of acoustic emissions (Tang, 1997). In this mode, the AE counts can be accounted for by the number of damaged elements and the energy releases can be calculated from the strain energy releases of damaged elements, which are the shadow area in Fig. 1. On the basis of this assumption, the cumulative AE counts and cumulative AE energy release can be realistically simulated with the above-mentioned numerical model.

The developed mesoscopic elemental mechanical model for elastic damage was fully implemented into the rock and tool interaction code (R-T^{2D}) on the basis of the finite element method, as shown in Fig. 3. In the code, the numerical specimen is constructed according to the heterogeneous material model (Liu, 2003) with the homogeneous index m and elemental seed parameters, such as the critical

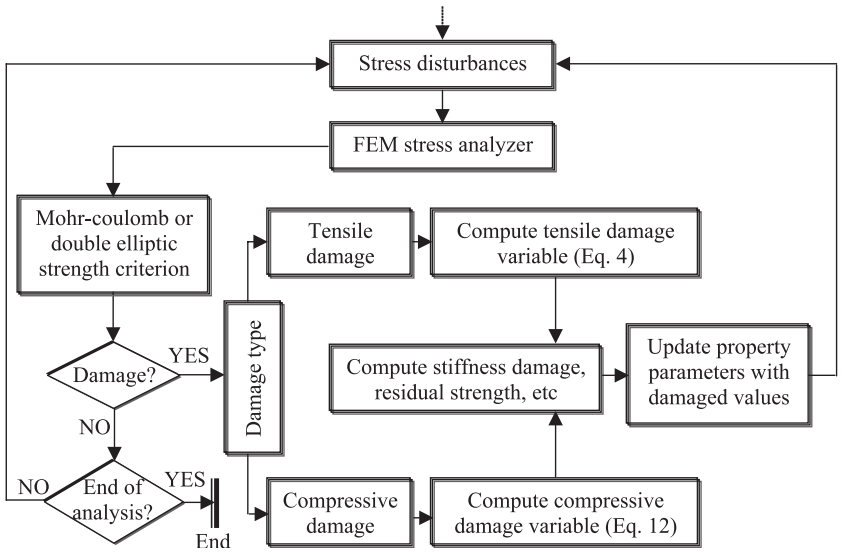

Fig. 3. Flowchart of the mesoscopic elemental model in the R-T^{2D} code.

strength σ_0, elastic modulus E_0, etc. During the loading process, the finite element method is used to compute the stress and deformation in each element, and the Mohr–Coulomb strength criterion or the double elliptic strength criterion (Liu et al., 2002) is used to examine whether or not elemental damage occurs. An external load is slowly applied on the constructed numerical specimen step by step. When in a certain step the stresses in some elements satisfy the strength criterion, the element is damaged and becomes weak according to the rules specified by the above-described mesoscopic elemental mechanical model for elastic damage. The stress and deformation distributions throughout the model are then adjusted instantaneously after each rupture to reach the equilibrium state. At positions with increased stress due to stress redistribution, the stress may exceed the critical value and further ruptures are caused. The process is repeated until no failure elements are present. The external load is then increased further. In this way the system develops a macroscopic fracture. Thus the code links the mesoscopic mechanical model to the continuum damage model and ultimately to macrostructure failure, which has been regarded as one of the most challenging tasks in the area of brittle failure micromechanics.

3. Failure process of a rock specimen under various confining pressures

3.1. Numerical model

Laboratory experiments on rock fracture in compression are normally carried out by loading cylindrical specimens in either uniaxial or triaxial conditions (ISRM, 1978; Kovari et al., 1983). Although an experimental system for a triaxial test in the laboratory can be very complicated, with respect to numerical modelling the interesting part is the core of the system, which consists mainly of a rock specimen and a pair of steel platens (Blair and Cook, 1998; Tang et al., 2000; Fang and Harrison, 2002b). The numerical model used in this paper represents the two-dimensional plane stress problem, as shown in Fig. 4. The model comprises a rock sample with a length-to-diameter ratio of 2.5 ($L/D=2.5$) and a pair of platens. Both the rock body and the platens are discretised into $54 \times 145 = 7830$ elements. The steel platens are simulated as homogeneous material, which deforms elastically and is not allowed to failure during the tests, while the rock sample is simulated as heterogeneous brittle material. Because of the heterogeneity, each element contains an unequal number of defects and therefore

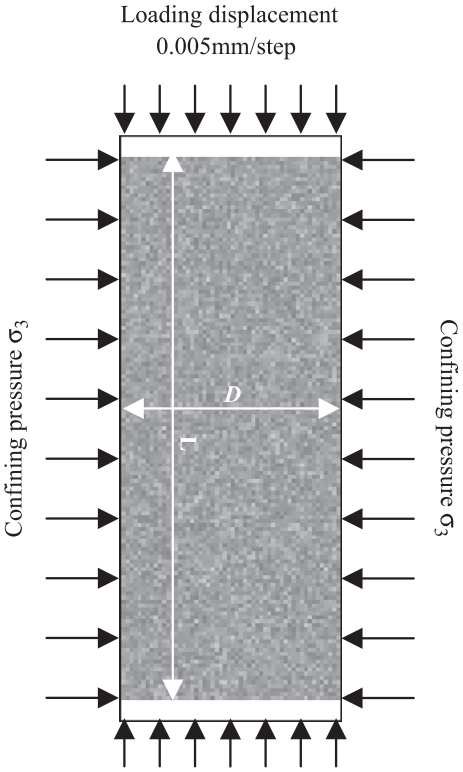

Fig. 4. Numerical model for a heterogeneous rock specimen under various confining pressures.

possesses different physical–mechanical parameters. Assume that the local physical–mechanical parameters are distributed following a certain probability distribution. On the basis of the previous work (Weibull, 1951; Hudson and Fairhurst, 1969), Weibull's distribution describes very well the experimental data for the distribution of micro-defects within rock. Here, we assume that the elemental physical–mechanical parameters follow the heterogeneous material model (Liu, 2003) on the basis of Weibull's distribution

$$\varphi(\omega) = \frac{m}{\omega}\left(\frac{\omega}{\omega_0}\right)^{m-1} \exp\left[-\left(\frac{\omega}{\omega_0}\right)^{m}\right] \qquad (14)$$

where ω is the elemental parameter, ω_0 is the mean value of the elemental parameter, i.e. the elemental seed parameters, such as the critical strength σ_0, elastic modulus E_0, etc., and m is the shape parameter describing the scatter of ω, which can be defined as the homogeneous index of the rock (Tang, 1997). The disorder of the probability distribution in physical space is achieved by the Monte Carlo method. Therefore, the method based on statistics and randomicity satisfies the requirements of heterogeneity and randomicity of element parameters in a finite element network of rock caused by mineralogy, porosity, grain size, grain orientation and grain boundary, etc., in real rock. However, the microstructural details in one given geometrical model of real rock are not taken into accounts, which requires further research work. In current simulations, the homogeneous index $m=2$ and the elemental seed parameters $\sigma_0=100$ MPa, $E_0=30$ GPa, etc., are used. Moreover, it is assumed that the Poisson's ratio $v_0=0.25$, the tensile/compressive strength ratio $\gamma=1/10$, the residual strength coefficient $\lambda=0.1$, the ultimate tensile strain coefficient $\eta=1.5$ and the re-compaction compressive strain coefficient $\xi=5$. To simplify the triaxial load application in the numerical experiments, an initial stress boundary is applied to the two sides of the rock specimen and the outer surfaces of both platens to achieve a hydrostatic stress state at the level of a specific confining pressure. This is followed by an incremental axial displacement (0.005 mm/step) of the platens to apply the axial stress. In the simulation of progressive failure of rock, the reason for using displacement-controlled loading instead of force-controlled loading is that displacement-controlled loading enables the simulation of the entire response spectrum of progressively failure media, including post-peak softening.

In the following, the failure processes of the constructed heterogeneous rock specimen subjected to confining pressures of 0, 20, 40 and 80 MPa under triaxial conditions are numerically simulated. It should be noted that the simulations in this section were performed using an identical set of properties for the rock specimen (including the individual element strength and the elastic modulus) and that only the confining pressure was varied. Since similar characteristics are observed at confining pressures of 20 and 40 MPa, we describe the failure process of the rock specimen under uniaxial compression, a moderate confining pressure and a high confining pressure by reference to confining pressures of 0, 20 and 80 MPa, respectively.

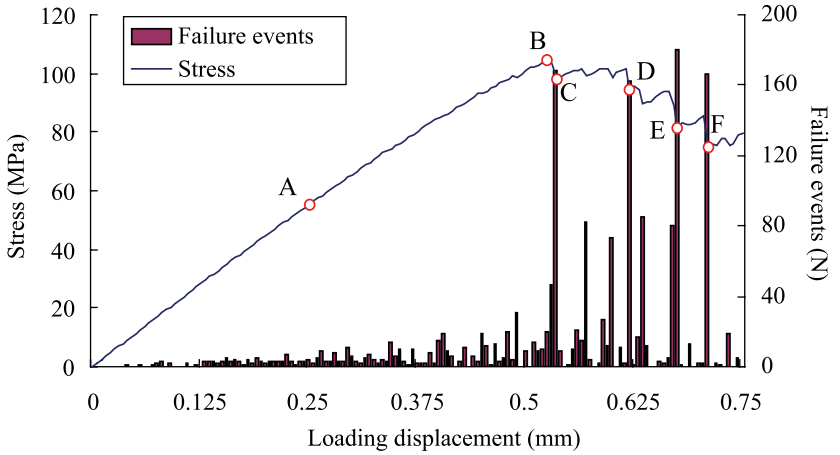

Fig. 5. Simulated stress–displacement curve and failure event rate of a rock specimen subjected to a confining pressure of 0 MPa.

3.2. Failure process of a rock specimen under uniaxial compression

Since a previous paper (Tang et al., 2000) discussed the failure process under uniaxial compression in detail, where, however, the Mohr–Coulomb strength criterion was used, here we just simply report the simulated results so that the comparison can be made in the subsequent fracture analysis under triaxial compression. Fig. 5 records the stress–displacement curve and the associated microseismicities' (failure events') temporal distributions for a rock specimen under uniaxial compression. The spatial distributions of the failure events at the different loading levels labelled by alphabetic letters, i.e. A, B, etc., in Fig. 5 are correspondingly depicted in Fig. 6. In the figure, the red (grey in a black–white picture) colour represents the tensile failure and the blue (dark in a black–white picture) colour represents the compressive failure at the current loading level. The black colour represents the accumulative tensile and compressive failure at the previous loading levels. At the linear elastic stage (curve before point A in Fig. 5), the failure events are randomly distributed throughout the specimen (Fig. 6A) because of the heterogeneity, reflecting the statistically uniform deformation during this portion of the simulation. At the non-linear deformation stage (curve AB in Fig. 5), though a few failure events are still occurring throughout the specimen, more failure events are now clustered to form a few active microseismic zones, which are marked by the ellipses in Fig. 6B.

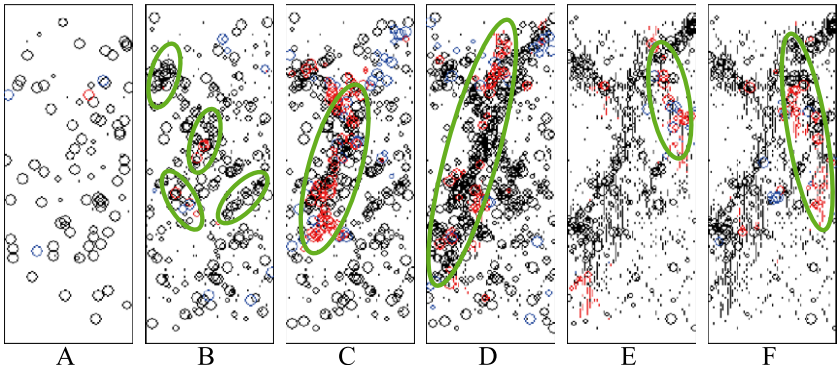

Fig. 6. Simulated spatial distribution of the failure event sequence in a rock specimen subjected to a confining pressure of 0 MPa.

The formed actively microseismic zones are the potential nucleation sites in the future failure process but it is difficult to predict where the macrofailure will initiate. After the peak load (Point B in Fig. 5, where the uniaxial compressive strength is $\sigma_c = 103.5$ MPa), there is a big stress drop (Point C in Fig. 5) in the stress–displacement curve and also a large number of active micro-seismic events localize in one of the potential nucleation sites to develop a macroscopic crack, which is marked by the ellipse in Fig. 6C. This is believed to be the result of stress distribution, redistribution and migration from the surrounding potential nucleation zones to the active microseismic zone, where a high stress is established. As the loading displacement increases, the stress–displacement curve continuously descends (Point D in Fig. 5D) and correspondingly the formed macroscopic fracture propagates along an inclined plane but approximately along the major principal stress direction, which is marked by the ellipse in Fig. 6D. It is found that during these stages, the failure event counts decrease in intensity throughout the rest of the specimen expect the macroscopic fracture plane. With continuous loading displacement, the stress–displacement curve continues dropping down to represent a typical brittle behaviour (Point E and F in Fig. 5) and another main fault plane is developed at the active microseismic zone, which is marked by ellipses in Fig. 6E and F. It is important to find, and undoubtedly of some seismological significance, that the highest AE event counts do not correspond to the maximal stress (Fig. 5B), but to the post-peak region (Figs. 5 and 6E), which is the new physical phenomena and has never been reported in literatures on the basis of laboratory investigations.

Fig. 7 shows the simulated initiation, propagation and coalescence of the cracks at different loading levels labelled in Fig. 5. The grey scale in the figure represents the value of the maximum principal stress. The brighter the colour, the higher the maximum principal stress. It can be seen that the onset of failure in the specimen subjected to uniaxial compressive loading is indicated first by the formation of a large number of isolated microfailures (Fig. 7A and B). The microfailures begin to cluster and become clearly localized in Fig. 7C, where a macroscopic crack comes into being. As the loading displacement increases, the formed macroscopic crack propagates in a direction sub-parallel to the maximum compressive axis and therefore a fault plane is formed (Fig. 7D). Hence, mode I cracking is the dominant mechanism. After that, another main macroscopic crack begins to grow (Fig. 7E). Finally the two main cracks propagate at the same time and two conjugated macroscopic fault planes develop (Fig. 7F).

3.3. Failure process of a rock specimen at a moderate confining pressure (20 MPa)

Fig. 8 illustrates the resultant stress–displacement curve and the temporal sequence of the associated failure event rates when loading the heterogeneous rock specimen under a moderate confining pressure, $\sigma_3 = 20$ MPa. Correspondingly, Fig. 9 records the spatial sequence of failure events in the specimen. The symbols in the figure have the same meaning as

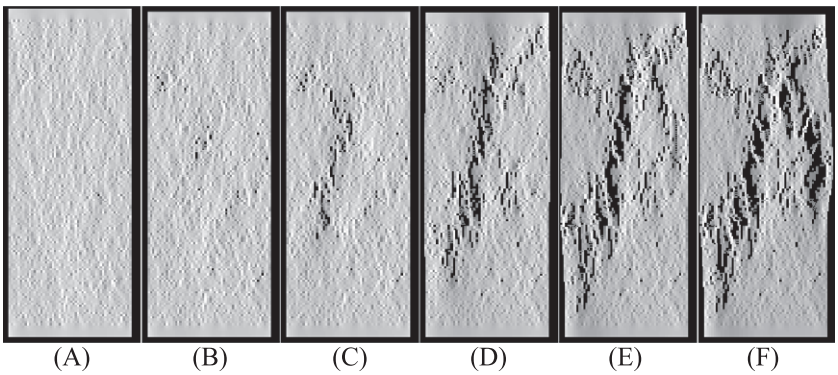

Fig. 7. Simulated maximum principal (compressive) stress distribution of a rock specimen subjected to a confining pressure of 0 MPa.

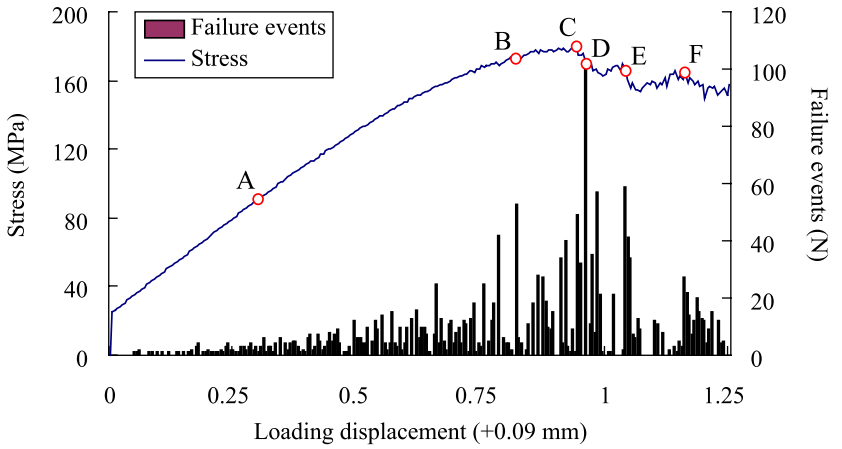

Fig. 8. Simulated stress–displacement curve and failure event rate of a rock specimen subjected to a confining pressure of 20 MPa.

those in Fig. 6. During the loading process, the confining pressure is applied on the rock specimen in the first loading step, and correspondingly an axial loading displacement (0.09 mm) is applied on the loading platen to achieve a hydrostatic stress state. Similar to the case of the uniaxial compression, at the linear elastic stage (curve before Point A in Fig. 8), the local failure events are initiated at various sparse sites (Fig. 9A) because of the heterogeneity. Then, at the non-linear deformation stage (curve ABC in Fig. 8) more individual failure events develop at a few microseismic zones, which are marked by the ellipses in Fig. 9B. Compared with the failure events shown by the histogram in Fig. 5, more failure events occur in the confined compression, which reveals that there is a more progressive non-linear deformation stage in confined compression than that in uniaxial compression. At the peak load (Point C in Fig. 8, where the compressive strength of the rock specimen under a confining pressures of 20 MPa is $\sigma_{c|20} = 180.2$ MPa), the diffused failed sites tend to become dense at the marked sites by ellipses in Fig. 9C. During this process, it is noticed that compressive failure is the main mechanism, whereas in uniaxial compression, tensile failure is the main mechanism, as shown by the red (grey in a black–white picture) colour in Fig. 6C. This explains why, with the continuous loading displacement, the cracks are formed by the linking of the failed sites (marked by the ellipse in Fig. 9D) instead of the extension of the current failure sites parallel to the major principal stress. At the same time, the failure events reach the maximum (Point D in Fig. 8) as shown by the histogram in Fig. 8 and correspondingly the stress-loading displacement curve descends rapid-

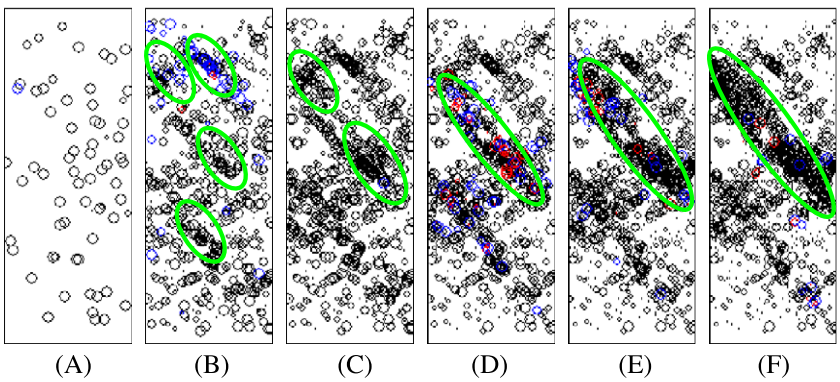

Fig. 9. Simulated spatial distribution of the failure event sequence in a rock specimen subjected to a confining pressure of 20 MPa.

ly. It is again noted that the maximum failure events count does not lay at the peak load but at the post failure stage, which is the new phenomena explored by numerical simulation. A subsequent increase in the loading displacement (Point E in Fig. 8) enhances the linkage between the failed sites to form a macroscopic shear fracture plane as marked by the ellipse in Fig. 9E. During this process, the extension of some linked cracks is observed to propagate parallel to the major principal stress, because the confining pressure is not so high. After that, more and more failure sites are formed in the macroscopic shear fracture marked by the ellipse in Fig. 9F, which causes the shear fracture plane to continue to grow until finally the formation of the macroscopic through-going shear fracture plane is complete.

Fig. 10 shows the simulated progressive failure processes in terms of the distribution of the major principal stress. Again it can be seen that the onset of failure in the specimen is indicated first by the formation of a large number of isolated microfailures (Fig. 10A). However, with the loading displacement increasing, one notices a behaviour different from the uniaxial compression case, where the failure sites propagate parallel to the major principal stress, namely that more individual failure sites tend to develop in the confined condition and it is only when the diffused failed sites become dense that extensile cracks begin to propagate from failed sites (Fig. 10C). A further increment in the loading displacement causes these cracks to tend to link with each other (Fig. 10D). A subsequent increase in the loading displacement enhances the linkage between the failed sites to form a macroscopic shear fracture plane (Fig. 10E). The shear fracture plane continues to grow, until finally the formation of the macroscopic through-going shear fracture plane is complete and the specimen fails completely on the macroscopic scale by a single shear fracture plane (Fig. 10F).

3.4. Failure process of a rock specimen at a high confining pressure (80 MPa)

Fig. 11 shows the corresponding stress–displacement curve and the associated failure event rate when loading the rock specimen at a high confining pressure, $\sigma_3 = 80$ MPa. In Fig. 12, we present the locations of the failure event sequences occurring during the loading stages. The symbols in the figure have the same meaning as the aforementioned. Moreover, the green (light grey in a black–white picture) colour represents ductile cataclastic failure, with the stresses of the element satisfying the ductile failure surface of the double elliptic strength criterion at the current loading level. The confining pressure is applied on the rock specimen in the first loading step, and correspondingly an axial loading displacement (0.36 mm) is applied on the loading platen to achieve a hydrostatic stress state. As shown in Fig. 11, the compressive strength of the rock specimen under a confining pressure of 80 MPa is $\sigma_{c|80} = 310.5$ MPa. Compared with the previous cases, as for the stress–displacement curve, the main difference lies in the post-failure stage (curve BCDEF in Fig. 11). The prominent characteristics of the post-failure stage under high confining pressure are volume condensation (as

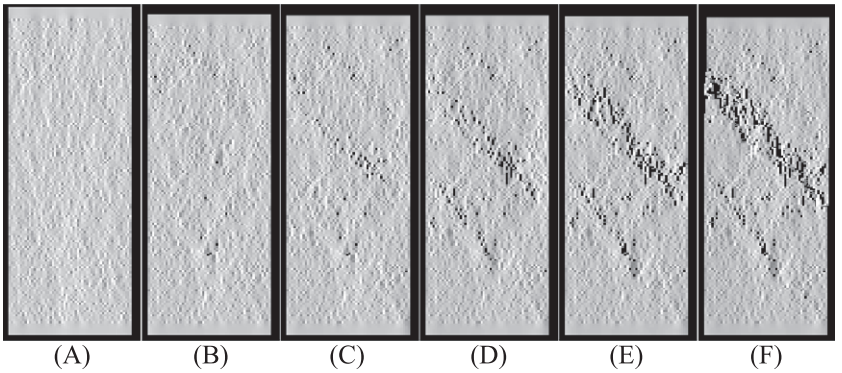

Fig. 10. Simulated maximum principal (compressive) stress distribution of a rock specimen subjected to a confining pressure of 20 MPa.

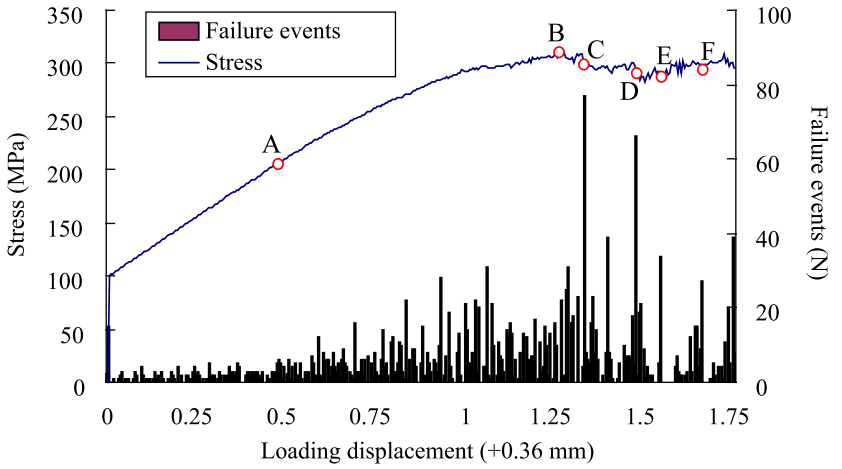

Fig. 11. Simulated stress–displacement curve and failure event rate of a rock specimen subjected to a confining pressure of 80 MPa.

shown later in Fig. 16) and a very small stress drop or no stress drop (Point C, D, E and F in Fig. 11). Therefore, the curve in Fig. 11 presents a plastic behaviour, which indicates that the stresses of some elements satisfy the ductile failure surface of the double elliptic strength criterion, because of the high confining pressure; and that the compressive strain of some failed elements in the shearing band attains the re-compaction compressive strain, so that a re-compaction behaviour occurs. As for the failure events, the main difference is that some of the elements fail in the ductile cataclastic mode, with the stresses satisfying the ductile failure surface of the double elliptic strength criterion, as shown by the green (light grey) colour in Fig. 12 because of the high confining pressure. Moreover, more failure events occur before the peak load (Point B in Fig. 11) and the maximum failure event rate (Point C in Fig. 11) becomes closer to the peak load point. The local shear band, marked by the ellipses in Fig. 12, is formed after the failed sites become dense and coalesce with each other.

Fig. 13 shows the simulated progressive failure processes in terms of the distribution of the major principal stress. In the quasi-linear deformation stage and non-linear deformation stage, the elemental failures are initiated at isolated locations (Fig. 13A and B). The failure sites are not clear in these figures because the large axial deformation makes the isolated cracks close. As the loading displacement increases, the failed sites become dense and a few sites extend short distances to form arrays of cracks (Fig. 13C). Then the failed sites begin to coalesce and form local

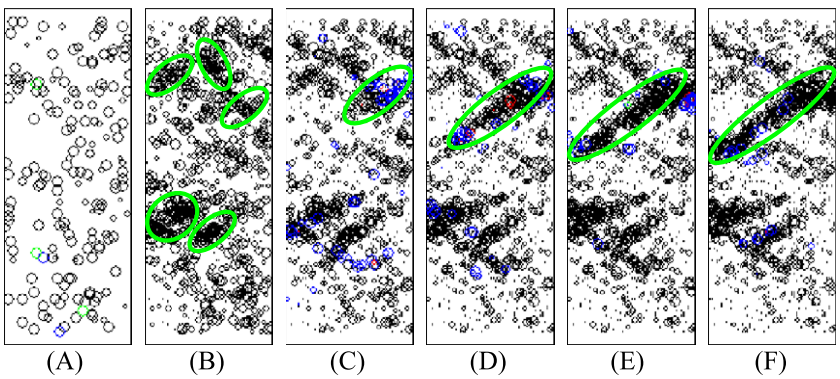

Fig. 12. Simulated spatial distribution of the failure event sequence in a rock specimen subjected to a confining pressure of 80 MPa.

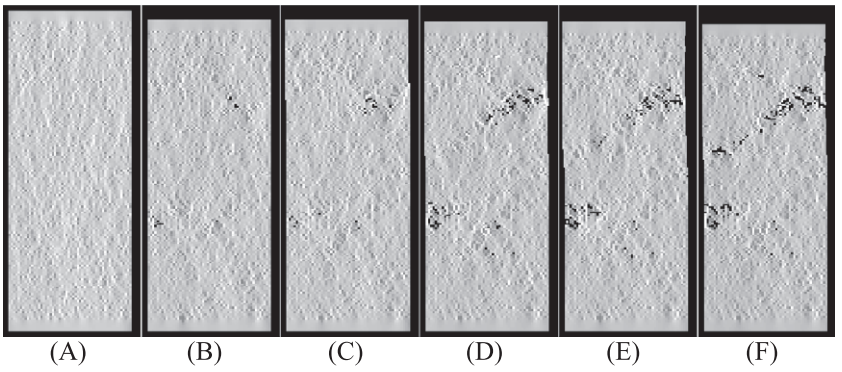

Fig. 13. Simulated maximum principal (compressive) stress distribution of a rock specimen subjected to a confining pressure of 80 MPa.

shear bands (Fig. 13D). Subsequently, a macroscopic shear band forms (Fig. 13E). Further increments in the axial displacement tend to re-establish the contact between the crack surfaces (Fig. 13F) and the material behaves in a ductile fashion. Compared with the previous cases (involving uniaxial compression and moderate confining pressure), the cracks in the specimen induced under a high confining pressure are closer, which indicates that the compressive strain of some elements in the shear band attains the re-compaction compressive strain and a re-compaction behaviour occurs.

4. Discussions

In Section 3, the progressive failure processes of the heterogeneous rock specimen under a wide range of confining pressures ($\sigma_3 = 0-80$ MPa) have been simulated using the developed mesoscopic elemental mechanical model for elastic damage. In the present section, the simulated results are discussed through a comparison with the laboratory data in the literature and the results simulated by other researchers.

4.1. Fracture development from the mesoscopic scale to the macroscopic scale

On the basis of the simulated failure event distributions shown in Figs. 6, 9 and 12), it can be concluded that local failure events are first randomly initiated at a load level well before the peak load (Figs. 6, 9 and 12A), with the stresses of the mesoscopic elements in the heterogeneous rock specimen satisfying the strength criterion. As the loading displacement increases, some of the failed sites extend in the direction of the major principal stress in the case of uniaxial compression and, in the case of confining pressure, more individual failure sites develop to connect with each other and hence cause crack arrays to form (Figs. 6, 9 and 12B). Further loading causes the coalescence of arrayed cracks and macroscopic cracks are formed (Figs. 6, 9 and 12C). Finally, the formed macroscopic cracks propagate and macroscopic through-going fracture planes develop (Figs. 6, 9 and 12D–F). Similar phenomena have been observed in laboratory tests (Wawersik and Fairhurst, 1970; Tapponnier and Brace, 1976). Preceding the rock fracture, mesoscopic processes start from random initiation and then develop through the extension of microcracks into the formation and coalescence of arrayed cracks. Moreover, the degree of crack extension is influenced by the magnitude of the confining pressure, in that the extension of failed sites is suppressed with increasing confining pressure. Using a degradation model coupled with FLAC (Itasca, 1995), Fang and Harrison (2002b) have also simulated the fracture development from the elemental scale to the macroscopic scale. Their results are consistent with our numerically simulated results. However, it is a pity that in their model the stress distribution and redistribution, and the displacement field are not simulated or shown.

The loss of homogeneity, i.e. the macroscopic crack, was observed to occur in the softening regime (Figs. 5C, 8D and 11C), i.e. after the peak stress. This

loss of homogeneity is recognized as being associated with the localisation phenomenon, as shown in Figs. 6 and 7C–F,Figs. 9 and 10D–F, and Figs. 12 and 13C–F, which is consistent with the laboratory results observed by other authors (Lockner et al., 1991; Labuz et al., 1996) indicating that shear bands become fully developed throughout the specimen only in the softening regime of the specimen's response.

4.2. Brittle to semi-brittle and ductile transitions

Failure in rock is generally characterised by a brittle regime, a transitional semi-brittle regime and a ductile regime (Besuelle et al., 2000). Fig. 14 collects the simulated stress–displacement curves obtained by the R-T^{2D} code at all the applied confining pressures used in the simulation, i.e. 0, 20, 40 and 80 MPa. It is shown that the mechanical behaviour of the specimen is greatly affected by the confining pressure. The deformation and failure are brittle, if the confining pressure is zero or relatively low. Under uniaxial compression, the fracture processes develop very quickly, so that the specimen collapses over a very small strain range, which is the brittle regime. In this case, there are three distinctive strengths, which split the whole deformation and failure process into four stages. The three strengths are the yield strength (Point A in Fig. 5), the limit strength (Point B in Fig. 5), and the residual strength (Point F in Fig. 5). The four stages are called the elastic region (the line in Fig. 5 before Point A), the initial damage region (AB in Fig. 5), the post-failure region (BCEDF in Fig. 5), and the shearing and slipping region, respectively. Dilation under a stress higher than the yield strength (as shown later in Figs. 15 and 16) and a post-failure stage with a descending load bearing capacity (Fig. 5) are the prominent characteristics in this case. At the post-failure stage, the stress–displacement curve of the sample experiences stress drops several times (Point C, D, E and F in Fig. 5) before the axial stress reaches a residual level, and the behaviour of the material is brittle. As the confining pressure increases (to 20 and 40 MPa), the strain hardening range (Fig. 8A,B,C) increases and both the strength loss after the peak and the brittleness of the curve decrease (Figs. 8 and 14). Finally, when the confining pressure increases to 80 MPa, the material behaviour becomes plastic (Figs. 11 and 14). The prominent characteristics, in this case, are volume condensation (as shown later in Fig. 16) and ductile cataclastic failure, with the stresses of some elements satisfying the ductile failure surface of the double elliptic strength criterion and with a constant or increasing load bearing capacity with increasing strain because of the ductile cataclastic failure and because the compressive strain of some elements exceeds the re-compaction compressive strain. In addition, the failed specimens with brittle failure have two conjugated inclined shear bands, but the remnants of the specimens with ductile failure are almost barrel-shaped. On the basis of the friction mechanism between crack surfaces, Kou (1995) explained the shape of the specimen remnant after

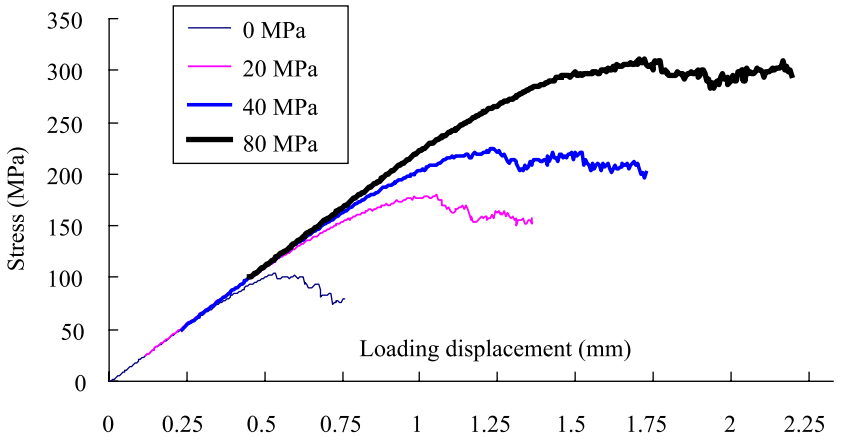

Fig. 14. Simulated stress–displacement curves of a rock specimen under various confining pressures.

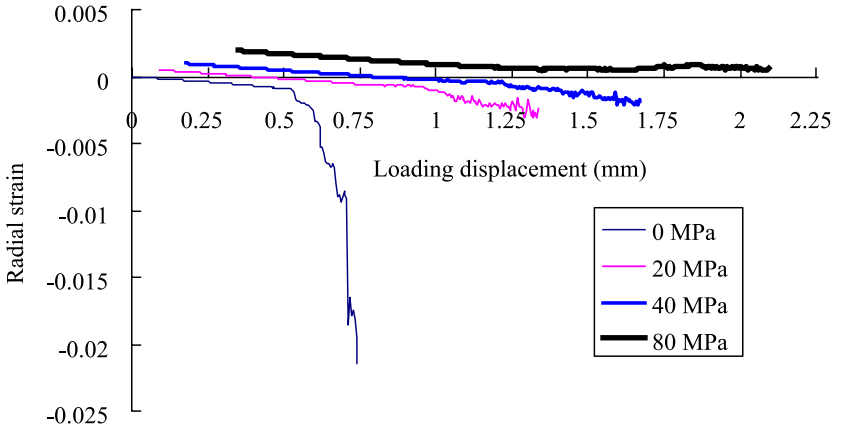

Fig. 15. Simulated radial strain versus loading displacement in compressing a rock specimen under various confining pressures.

testing. In the brittle case, the material plane along the crack becomes weak compared with other possible planes, and the crack is prone to grow in that plane. This is the case where the bearing capacity of the specimen decreases progressively during the formation of the shearing band. The shearing band in the specimen, once formed, splits the specimen into two parts, and, due to stress relief, each of them may be treated as rigid. The specimen deformation is then induced by the relative slip between the two rigid parts. In the ductile case, however, the plane along the cracked surface becomes stronger than the other possible shear planes and unfavourable to crack growth. The specimen remnant becomes barrel-shaped due to the action of stresses and friction from the two loading platens. Therefore, confining stress has an important influence on the mechanical properties of rock.

The numerically simulated results are consistent with the laboratory observations in triaxial experiments (Wawersik and Fairhurst, 1970; Brady and Brown, 1992; Weijermars, 1997), indicating that the confining pressure influences the non-linearity of the stress–strain curve. As the confining pressure increases, the peak strength increases, the hardening range widens and the strength drop in the softening (i.e. post-peak) range decreases, with the material becoming plastic when the confining pressure is sufficiently large. It should be noted that the only variable in the simulation used to produce Fig. 14 is the confining pressure, and that all the other model parameters are identical across all the simulations.

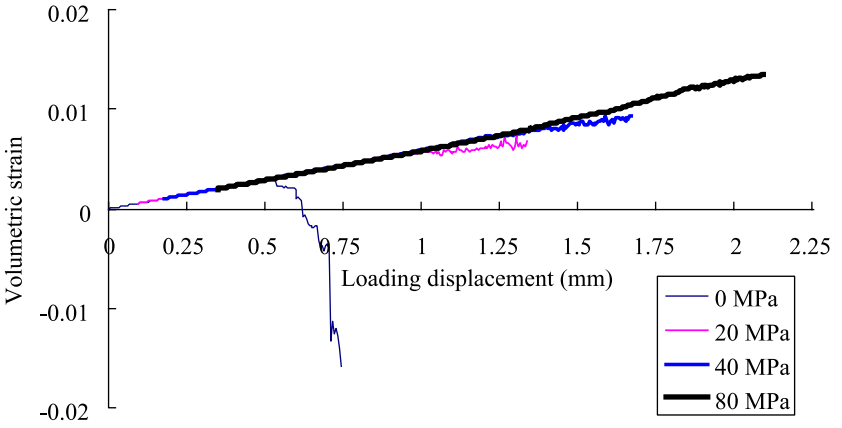

Fig. 16. Simulated volumetric strain versus loading displacement in compressing a rock specimen under various confining pressures.

Therefore, a comparison between numerical simulations and laboratory observations in the literature shows that the mesoscopic mechanical model is capable of reproducing the whole range of stress–strain curves, from brittle to plastic, displayed by rock subjected to various confining pressures.

Figs. 15 and 16 show the radial strain and the volumetric strain, respectively, versus the loading displacement in compressing the rock specimen at various confining pressures (0, 20, 40 and 80 MPa). Because the confining pressures are applied on the rock specimen in the first step and corresponding axial loading displacements are applied on the loading plates to achieve the hydrostatic stress state, we do not have the loading history until the axial stress is larger than the confining pressure. After the confining pressures are applied on the rock, the maximum contractional radial strains are induced in all the cases (Fig. 15). In the case of uniaxial compression, firstly the dilatant radial strain gradually increases as the axial loading displacement increases. Then after the peak load (Fig. 5B), the dilatant axial strain dramatically increases in the post-failure stage. Under moderate confining pressures (20 and 40 MPa), the contractional radial strain is induced before the non-linear deformation stage, but its value becomes smaller and smaller with increasing axial loading displacement. In the non-linear deformation stage, the contractional radial strain gradually becomes the dilatant radial strain. After the peak stress, an increase in the dilatant radial strain is observed. However, under high confining pressure (80 MPa), the contractional radial strain is always induced during the whole loading process, although its value becomes smaller and smaller and finally seems to keep a small constant value as the loading displacement increases. As far as the volumetric strain versus the loading displacement curves is concerned (Fig. 16), one observes first that an initial contraction is induced at all confining pressures, including the uniaxial compression case, and increases with increasing axial loading displacement. Then up to the peak stress, depending on the confining pressure, one obtains either dilatancy under uniaxial compression, or contraction at the moderate and the highest confining pressure. Moreover, the contractional volumetric strain under the high confining pressure increases faster than that under the moderate confining pressure in the post-failure stage. A similar evolution has been observed in laboratory tests on porous rocks (Cornet and Fairhurst, 1974) and coal (Kou, 1995). Therefore, the comparisons between the induced radial and volumetric strain inside the specimens during the triaxial compression tests show a relative dilatancy in the brittle regime, but a relative contraction, so-called "shear-enhanced compaction", in the semi-brittle regime and a high compactancy in the ductile regime (Wong et al., 1997).

It is noted that the compacting shear bands under high confining pressures are simulated very well by the R-T^{2D} code. Compacting shear bands could have important implications in field applications, which have been a challenging subject in the context of the theoretical analysis of localisations by bifurcation theory (Besuelle et al., 2000). For example, local permeability reduction in a layer or a set of parallel layers produced as a result of localisation could produce important changes in the permeability of a global structure (Besuelle et al., 2000).

4.3. Fracture patterns and fracture plane angles

Fig. 17 shows a comparison of the typical patterns of shear bands observed in laboratory tests (taken from Fang and Harrison, 2002b), simulated by the local degradation model (Fang and Harrison, 2002b) and simulated by the R-T^{2D} code in this paper, corresponding to the various confining pressures. We observe that in all the tests the specimens have failed with the appearance of one or several shear bands through the specimen. In Section 3, we have shown that the coalescence of cracked or weakened sites leads to the formation of eventual fracture planes or shear bands within a rock specimen under compression. In uniaxial compression, the collapse of a rock specimen is manifested by extensile fracture parallel to the applied stress, and a combination of axial splitting and inclined failure surfaces is observed (Fig. 17(iii), A). At moderate confining pressures, the eventual failure of the specimen is mainly characterized by one or more shear fracture planes (Fig. 17(iii), B and C). At higher confining pressures, the appearance of intense deformation is exhibited by a ductile region, and the shear fracture plane becomes narrow compared with that under a low confinement (Fig. 17(iii), D). Compared with the laboratory results (Fig. 17(i)) and the results simulated by other researchers

(A) Unconfined (B) Moderately confined (C) Confined at 80 MPa

i) Experimental results (taken from Fang and Harrison, 2002b)

(A) 0 MPa (B) 40 MPa (C) 80 MPa

ii) Simulated results using the local degradation model (Fang and Harrison, 2002b)

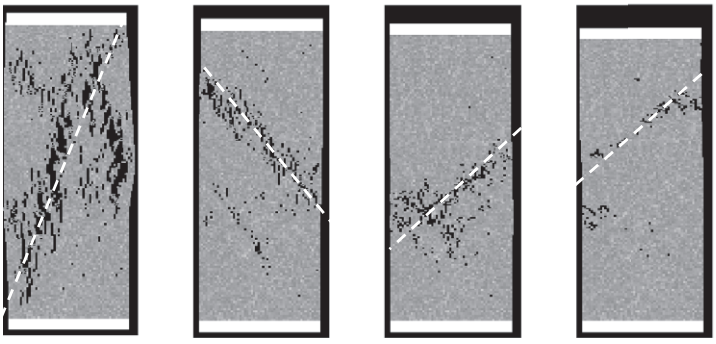

(A) 0 MPa (B) 20 MPa (C) 40 MPa (D) 80 MPa

iii) Simulated results using R-T^{2D} code (The grey scales represent different value of the elastic modulus, and the brighter the colour is, the higher is the value of the elastic modulus)

Fig. 17. Observed shear band patterns of real and simulated rock under various confining pressures.

(Fig. 17(ii)), the numerical simulation in this paper captures the essence of the features observed in laboratory tests and is consistent with the simulation performed by others though the rock type is different in the laboratory results.

According to the simulated eventual fracture planes in Fig. 17(iii) under confining pressures of 0, 20, 40 and 80 MPa, respectively, the orientation of the shear bands with respect to the loading axis increases with the confining pressure. A splitting fracture goes through the specimen in uniaxial compression (Fig. 17(iii), A) and a sharp shear fracture forms at a small angle to the major principal stress at a confining pressure of 20 MPa (Fig. 17(iii), B). A noticeable increase in the angle is seen at a confining pressure of 40 MPa (Fig. 17(iii), C). When the confining pressure

Table 1
Peak strengths under various confining pressures

Confining pressures	0 MPa	20 MPa	40 MPa	80 MPa
Simulated peak strength	103.5	180.2	224.0	310.5
Theoretical peak strength	103.5	163.5	223.5	343.5

increases to 80 MPa, the angle of the shear plane of the specimen increases a little further (Fig. 17(iii), D). Quantitatively, using a protractor to measure the orientations of the fracture planes in Fig. 17(iii) to the major principal stress, the fracture plane angles are about 20°, 37°, 45° and 47°, corresponding to confining pressures of 0, 20, 40 and 80 MPa, respectively.

Theoretically, the orientation of the shear band with respect to the major principal stress can be predicted by Mohr's model to be $\theta = 45° - \phi/2$, where ϕ is the internal friction angle of the material (Paterson, 1978). In this paper, the double elliptic strength criterion, which has a non-linear failure envelope, is adopted to check if the rock material will fail. In this kind of material with a non-linear fracture envelope, in the case of the Mohr orientation, ϕ should be defined as the angle of the failure envelope in the stress state corresponding to the failure, which is the orientation of the more critical plane, i.e. the plane of the stress state in the Mohr circle which first touches the failure envelope (Besuelle et al., 2000). Table 1 summarizes the simulated peak stresses corresponding to confining pressures of 0, 20, 40 and 80 MPa, which are 103.5, 180.2, 224.0, and 310.5 MPa, respectively. The theoretical peak stresses of a rock specimen under confining pressures of 0, 20, 40 and 80 MPa can be calculated according to the Mohr–Coulomb strength criterion $\sigma_1 = \sigma_c + \sigma_3(1 + \sin\ \phi)/(1 - \sin\ \phi)$, which are 103.5, 163.5, 223.5, and 343.5 MPa, respectively. Quantitative comparisons between the numerical and theoretical peak strength indicate that the numerical simulation also captures some kinds of quantitative aspects of rock failures in triaxial compression. Fig. 18 shows the predicted failure envelope in the Mohr diagram. The curve tangent to the Mohr circle of the triaxial compression test at the different confining pressures has an almost elliptic shape, and the slope of the failure envelope at the high confining pressure is expected to become negative, which shows that it is reasonable to use the double elliptic strength criterion to assess the critical stress. In Fig. 18, the straight lines show the inclination of the curve tangent to the Mohr circles of the different triaxial compressions tests. This Mohr prediction of the angle of the shear bands gives angles of about 25°, 30°, 34° and 40° at confining pressures of 0, 20, 40 and 80 MPa, respectively.

Fig. 19 schematically shows a comparison between the orientations of the fracture planes predicted by the mesoscopic mechanical model, the Mohr model and Ramez's experiments (Ramez, 1967). The simulated results by the mesoscopic mechanical model show the same trend as the results obtained with the Mohr model and Ramez's experiments, i.e. the fracture angle increases with increasing confining pressure. Moreover, our simulated results are consistent with those predicted by Fang and Harrison (2002b).

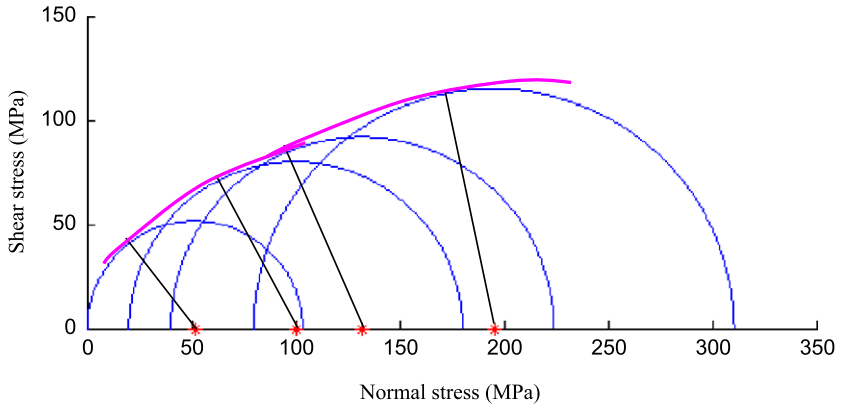

Fig. 18. Failure envelope in the Mohr diagram: the lines show the inclination of the curve tangent to the Mohr circles of the different triaxial compression tests.

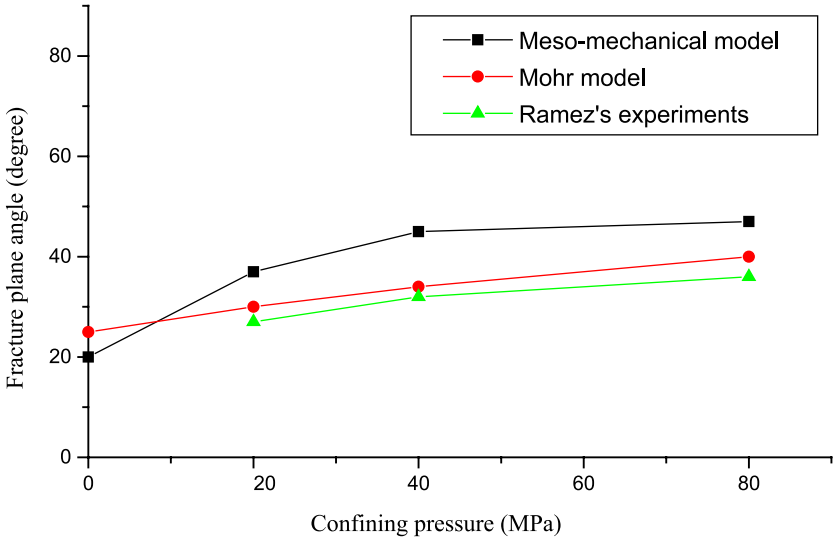

Fig. 19. Orientation of the fracture plane with respect to the major principal stress axis versus the confining pressures at failure.

4.4. Energy dissipation characteristics

The temporal sequences of the failure event rates (AE) in the rock specimen subjected to confining pressures of 0, 20 and 80 MPa were previously shown in Figs. 5, 8 and 11). It can be noted that in general AE events are not noticeable until the occurrence of non-linearity in the stress–displacement curve, and that the rate at which the AE events appear changes with the development of the fracture. The AE event rate increases gradually with the extension of the cracks, and increases rapidly as the cracks link together. The rate maximises when the final fracture planes form, which usually occurs in the post-peak region of the stress–displacement curve instead of at the peak load. Moreover, as the confining pressure increases, the position of the maximum failure events rate moves towards the peak load (Figs. 5E, 8D and 11C). Figs. 6, 9 and 12) show the spatial sequence of the failure event rates in the rock specimen subjected to confining pressures of 0, 20 and 80 MPa. It is observed that at the first stage, the events are distributed throughout the specimen, reflecting the statistically uniform deformation during this portion of the simulation. It is difficult to predict where the macrofracture will initiate in this stage. Then failure events are clustered near the zone that seems to be the potential nucleation site, or the diffused failed sites become dense. A subsequent increase in the loading displacement makes the nucleated sites extend in the direction of the major principal stress or enhances the linkage between the failed sites, and a macroscopic shear fracture band is formed. Finally, most of the failure events occur in the macroscopic shear fracture band.

Correspondingly, associated with these failure events, there are elastic energy releases (ENR). Fig. 20 presents the simulated elastic energy releases and accumulated elastic energy releases during the fracture process of the rock specimen subjected to confining pressures of 0, 20, 40 and 80 MPa. It is observed that, although there are scattered failure events in the linear deformation stage because of the heterogeneity, little energy is released. With an increasing failure event rate in the non-linear deformation stage, there is an increase in the elastic energy release. The number of failure events increases rapidly with the coalescence of cracks in the post-failure stage. Correspondingly, the elastic energy release attains its maximum value when the eventual fracture plane forms. It is again noticed that the maximum rate of failure events and the maximum elastic energy releases appear in the post-peak range. A comparison of the energy dissipations shows that more and more energy is dissipated in the non-linear deformation stage as the confining pressure increases. Quantitatively, the ener-

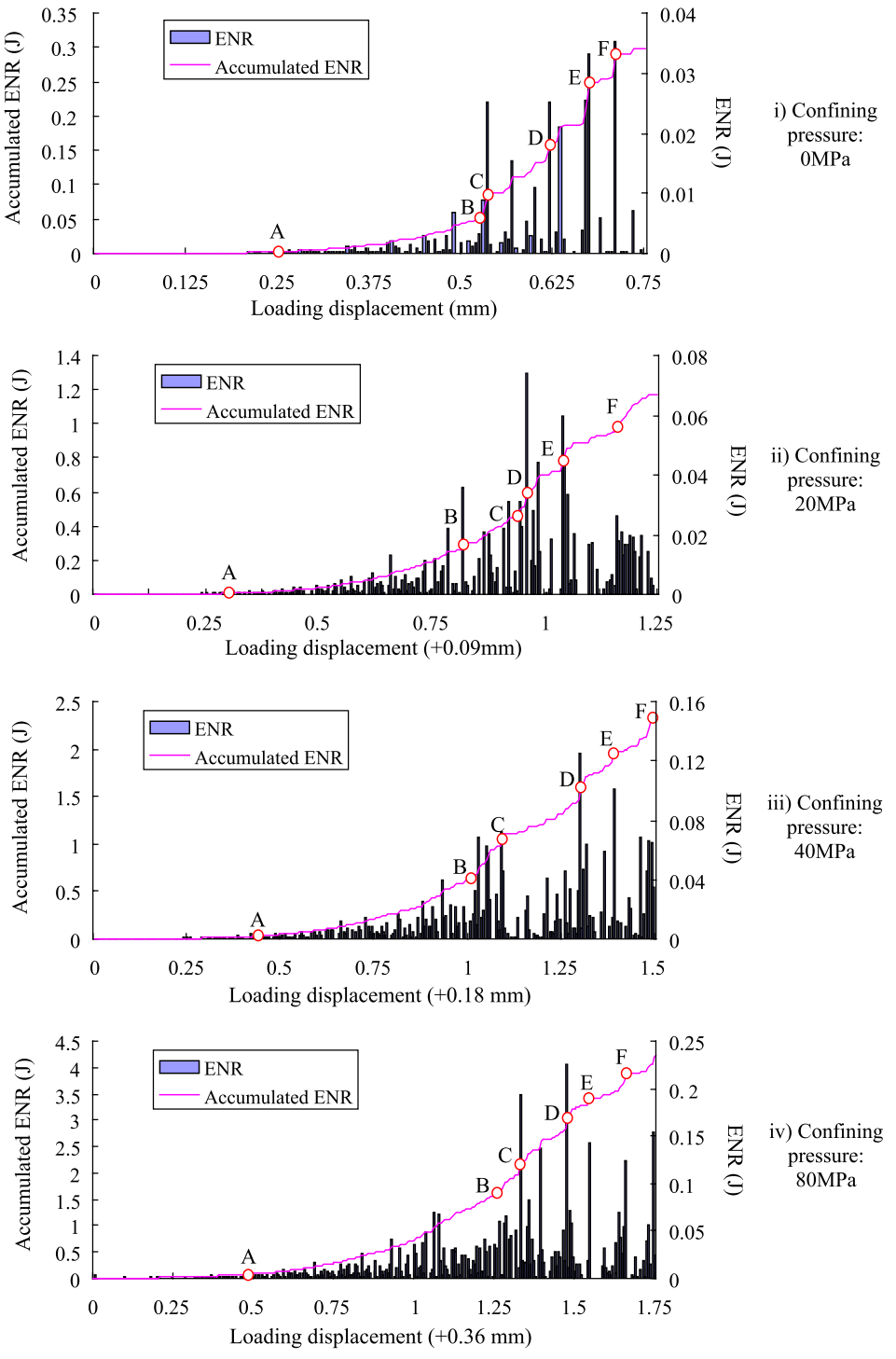

Fig. 20. Simulated elastic energy release (ENR) and accumulated ENR in compressing a rock specimen under various confining pressures.

gy dissipated in the non-linear deformation stage is 16.4% (Fig. 20(i), AB), 24.7% (Fig. 20(ii), ABC), 25.5% (Fig. 20 (iii), AB) and 36.7% (Fig. 20(iv), AB) of the total dissipated energy for the rock specimen subjected to confining pressures of 0, 20, 40 and 80 MPa, respectively. Correspondingly, less and less energy is dissipated by the post-failure stage with increasing confining pressure, i.e. 82.7%, 74.8%, 73% and 61.4% of the total dissipated energy in the cases involving confining pressures of 0, 20, 40 and 80 MPa, respectively.

5. Conclusions

The study of brittle fracture process and associated seismicity in rock under compression is essential for an understanding of many processes encountered in rock engineering and earth sciences. In this paper, firstly the mesoscopic elemental mechanical model for elastic damage is developed and coupled into the rock and tool interaction code (R-T^{2D}) on the basis of the finite element method. Then the triaxial compression test of a constructed heterogeneous rock specimen is numerically investigated using the developed mesoscopic mechanical model. Finally, the fracture development from the mesoscopic scale to the macroscopic scale, the stress–displacement curve, the radial and volumetric strain–displacement curve, the fracture pattern and fracture plane angle, and the energy dissipation characteristic obtained during the simulation of triaxial tests are discussed.

The examples presented and discussed herein demonstrate the power and versatility of the developed model. On the basis of the simulated results, it is found that in triaxial tests, at first the local failures are randomly initiated at a load level well before the peak load because of the heterogeneity. As the loading displacement increases, in the case of uniaxial compression, the local failure development is mainly manifested by the extension of failed sites in the direction of the major principal stress, with the final failure of the rock specimen being induced by a combination of axial splitting and shearing. Dilatancy and a post-failure stage with a descending load bearing capacity (brittleness) are the prominent characteristics and tensile failure is the dominantly mechanism. In the case of moderate confining pressure, the extension of the failed sites is suppressed, but the individual failure sites become dense and link with each other to form a shear fracture plane. The strain hardening range, the peak strength, the residual strength and the fracture plane angle increase, and the stress–strain behaviour becomes more ductile with confining pressure increasing. When the confining pressure is sufficiently large, some of the elements fail in ductile cataclastic mode with the stresses satisfying the ductile failure surface of the double elliptic strength criterion and some of the failed elements are re-compacted as the compressive strain attains the re-compaction compressive strain. Correspondingly, the stress–strain relation becomes plastic and the specimen fails through the deformation of a narrow shear zone. The prominent characteristics are volume condensation and ductile behaviour, with a constant or increasing load-bearing capacity with increasing strain. It should be noted that because of rock heterogeneity, the position of the highest microseismic events locates in the post-failure stage instead of the maximal stress but that position moves towards the peak load with confining pressure increasing. Though there are a large number of microseismic events before the peak load, few energies are dissipated. As the confining pressure increases, the microseismic events in the non-linear deformation stage increase dramatically, and the ratio between the energies dissipated by the non-linear deformation stage and those dissipated in the whole loading process increases correspondingly.

Therefore, it is concluded that the developed mesoscopic elemental mechanical model for elastic damage is able to reproduce the failure characteristics in loading rock specimens under triaxial compression, and the numerical modelling can furthermore obtain some new clarifications of the rock fracture process. Moreover, this kind of progressive process numerical model, which avoids the drawback of most quasi-static experiments that capture only the final failure pattern due to unstable crack growth, is more useful to research fracture process.

Acknowledgements

The financial support from LKAB's Foundation for the Promotion of Research and Education at Luleå

University of Technology, Trelleborg AB's Research and Education Foundation, the Foundation for Technology Transfer, Arne S. Lundberg's Foundation, and the Knowledge Foundation is greatly appreciated. Also, the authors would like to thank the two reviewers for their valuable comments and constructive suggestions on the manuscript.

Appendix A. The transformation related to the double elliptic strength criterion

At Point A in Fig. 2, the stress condition is the triaxial tensile limiting stress state. In practice, it is very difficult to attain the triaxial tensile limiting stress state. Therefore, the uniaxial tensile strength σ_t is used here as an approximate tensile threshold, i.e.

$$\sigma_1 = \sigma_3 = -\sigma_t \tag{A-1}$$

Thus,

$$\sigma_g = \sigma_1 + \sigma_3 = -2\sigma_t \text{ and } \tau_g = \sigma_1 - \sigma_3 = 0 \tag{A-2}$$

At Point B in Fig. 2, the stress condition is the uniaxial compressive limiting stress state, i.e.

$$\sigma_1 = \sigma_c \text{ and } \sigma_3 = 0 \tag{A-3}$$

Thus,

$$\sigma_g = \sigma_1 + \sigma_3 = \sigma_c \text{ and } \tau_g = \sigma_1 - \sigma_3 = \sigma_c \tag{A-4}$$

Substituting Eqs. (A-2) and (A-4) into the brittle failure surface of the double elliptic strength criterion in Eq. (7), we can obtain the following group of equations:

$$\begin{cases} 2a\sigma_t - 2b\sigma_t = c \\ \sqrt{5}a\sigma_c + b\sigma_c = c \end{cases} \tag{A-5}$$

Combining the above equations, we can represent the brittle failure conditions in the double elliptic strength criterion as follows:

$$\frac{(2\gamma+1)\sqrt{\sigma_g^2 + 4\tau_g^2} + (2\gamma - \sqrt{5})\sigma_g}{2\gamma(1+\sqrt{5})} = \sigma_c \tag{A-6}$$

where $\gamma = \sigma_t/\sigma_c$ is the ratio between the uniaxial tensile strength and the uniaxial compressive strength.

After the elemental stresses satisfy the brittle failure surface of the double elliptic strength criterion, the element will fail. Then the element will have the residual strength σ_{cr}. In Eq. (A-6), substituting the elemental strength σ_c with the residual strength σ_{cr}, the following equation is obtained

$$\frac{(2\gamma+1)\sqrt{\sigma_g^2 + 4\tau_g^2} + (2\gamma - \sqrt{5})\sigma_g}{2\gamma(1+\sqrt{5})} = \sigma_{cr} \tag{A-7}$$

Noting that $\sigma_g = \sigma_1 + \sigma_3$ and $\tau_g = \sigma_1 - \sigma_3$, the major principal stress σ_1 can be represented as follows after the element fails:

$$\begin{aligned} \sigma_1 = {} & \frac{1}{2\gamma(4\gamma+5+\sqrt{5})}\Big\{2\sigma_3[4\gamma^2 + (3-\sqrt{5})\gamma + 2] \\ & + \gamma\sigma_{cr}[-2(1+\sqrt{5})\gamma + 5 + \sqrt{5}] \\ & + sqrt\Big\{16\sigma_3^2[-4(1+\sqrt{5})\gamma^3 - 4\sqrt{5}\gamma^2 \\ & + (3-\sqrt{5})\gamma + 1] + 8\gamma\sigma_3\sigma_{cr}[-8(1+\sqrt{5})\gamma^3 \\ & + 4(3-\sqrt{5})\gamma^2 + 2(9+\sqrt{5})\gamma + (5+\sqrt{5})] \\ & + 10(3+\sqrt{5})\gamma^2\sigma_{cr}^2(4\gamma^2 + 4\gamma + 1)\Big\}\Big\} \end{aligned} \tag{A-8}$$

Therefore, when the brittle failure surface of the double elliptic strength criterion is met, the maximum compressive principal strain ε_{c0} at the peak value of the maximum principal stress is calculated as follows:

$$\begin{aligned} \varepsilon_{c0} = {} & \frac{1}{E_0}[\sigma_1 - \nu(\sigma_2 + \sigma_3)] \\ = {} & \frac{1}{E_0}\Bigg\{-\nu(\sigma_2+\sigma_3) + \frac{1}{2\gamma(4\gamma+5+\sqrt{5})} \\ & \times \Big\{2\sigma_3[4\gamma^2 + (3-\sqrt{5})\gamma + 2] \\ & + \gamma\sigma_{cr}[-2(1+\sqrt{5})\gamma + 5 + \sqrt{5}] \\ & + sqrt\Big\{16\sigma_3^2[-4(1+\sqrt{5})\gamma^3 - 4\sqrt{5}\gamma^2 \\ & + (3-\sqrt{5})\gamma + 1] + 8\gamma\sigma_3\sigma_{cr}[-8(1+\sqrt{5})\gamma^3 \\ & + 4(3-\sqrt{5})\gamma^2 + 2(9+\sqrt{5})\gamma + (5+\sqrt{5})] \\ & + 10(3+\sqrt{5})\gamma^2\sigma_{cr}^2(4\gamma^2 + 4\gamma + 1)\Big\}\Big\}\Bigg\} \end{aligned} \tag{A-9}$$

References

Ayling, M.R., Meredith, P.G., Murrell, S.A.F., 1995. Microcracking during triaxial deformation of porous rocks monitored by changes in rock physical properties. I: elastic-wave propagation measurements on dry rocks. Tectonophysics 245, 205–221.

Besuelle, P., Desrues, J., Raynaud, S., 2000. Experimental characterization of the localization phenomenon inside a Vosges sandstone in a triaxial cell. Int. J. Rock Mech. Min. Sci. 37, 1223–1237.

Blair, S.C., Cook, N.G.W., 1998. Analysis of compressive failure in rock using statistical techniques. Part I: a non-linear rule-based model. Int. J. Rock Mech. Min. Sci. 35, 837–848.

Brady, B.H.G., Brown, E.T., 1992. Rock Mechanics for Underground Mining, 2nd ed. Chapman & Hall, London, p. 571.

Cerrolaza, M., Garcia, R., 1997. Boundary elements and damage mechanics to analyse excavations in rock mass. Eng. Anal. Bound. Elem. 20, 1–16.

Cornet, F.H., Fairhurst, C., 1974. Influence of pore pressure on the deformation behaviour of saturated rocks. Advances in Rock Mechanics: Proceedings of the Third Congress of the International Society for Rock Mechanics, vol. 2, Part A. National Academy of Sciences, Washington, DC, pp. 638–644.

Cox, S.J.D., Meredith, P.G., 1993. Microcrack formation and material softening in rock measured by monitoring acoustic emissions. Int. J. Rock Mech. Min. Sci. 30 (1), 11–24.

Fanella, D., Krajcinovic, D., 1988. A micromechanical model for concrete in compression. Eng. Fract. Mech. 29, 49–66.

Fang, Z., Harrison, J.P., 2002a. Development of a local degradation approach to the modelling of brittle fracture in heterogeneous rocks. Int. J. Rock Mech. Min. Sci. 39, 443–457.

Fang, Z., Harrison, J.P., 2002b. Application of a local degradation model to the analysis of brittle fracture of laboratory scale rock specimens under triaxial conditions. Int. J. Rock Mech. Min. Sci. 39, 459–476.

Hoek, E., Brown, E.T., 1980. Underground Excavations in Rock. Balkema, Rotterdam, p. 215.

Hori, M., Morihiro, H., 1998. Micromechanical analysis on deterioration due to freezing and thawing in porous brittle materials. Int. J. Eng. Sci. 36 (4), 511–522.

Hudson, J.A., Fairhurst, C., 1969. Tensile strength, Weibull's theory and a general statistical approach to rock failure. The Proceedings of the Civil Engineering Materials Conference, Southampton. Wiley Interscience, pp. 901–904.

ISRM, 1978. Suggested methods for determining the uniaxial compressive strength and deformability of rock materials. Int. J. Rock Mech. Min. Sci. 16, 137–140.

Itasca, 1995. Fast Lagrangian analysis of continua. Version 3.3, Minnesota.

Kawakata, H., Cho, A., Kiyama, T., Yanagidani, T., Kusunose, K., Shimada, M., 1999. Three-dimensional observations of faulting process in Westerly granite under uniaxial and triaxial conditions by X-ray CT scan. Tectonophysics 313, 293–305.

Kou, S.Q., 1995. Some basic problems in rock breakage by blasting and by indentation. PhD thesis, Luleå University of Technology, 180 D.

Kovari, K., Tisa, A., Einstein, H.H., Franklin, J.A., 1983. Suggested methods for determining the strength of rock materials in triaxial compression: revised version. Int. J. Rock Mech. Min. Sci. 20, 283–290.

Kranz, R.L., 1983. Microcracks in rocks: a review. Tectonophysics 100, 449–480.

Labuz, J.F., Dai, S.T., Papamichos, E., 1996. Plane-strain compression of rock-like materials. Int. J. Rock Mech. Min. Sci. 33, 273–284.

Lai, H.H., Lindqvist, P.-A., Rånman, K.-E., 1980. Reconsolidation of crushed rock fragments under a button indenter. TULEA, vol. 21. Luleå University of Technology, Luleå, Sweden, p. 32.

Lee, X., Ju, J.W., 1991. Micromechanical damage models for brittle solids: Part II. Compressive loadings. J. Eng. Mech. 117, 1515–1536.

Lemaitre, J., 1992. A Course on Damage Mechanics. Springer, Berlin.

Lindqvist, P.-A., 1982. Rock fragmentation by indentation and disc cutting: some theoretical and experimental studies. PhD thesis, Luleå University of Technology, 20 D.

Liu, H.Y., 2003. Numerical modelling of the rock fracture process under mechanical loading. Licentiate thesis, Luleå University of Technology, 04.

Liu, H.Y., Kou, S.Q., Lindqvist, P.-A., 2002. Numerical simulation of the fracture process in cutting heterogeneous brittle material. Int. J. Numer. Anal. Methods Geomech. 26, 1253–1278.

Lockner, D.A., Byerlee, J.D., Kuksenko, V., Ponomarev, A., Sidorin, A., 1991. Quasi-static fault growth and shear fracture energy in granite. Nature 350 (7), 39–42.

Lockner, D.A., Byerlee, J.D., Kuksenko, V., Ponomarev, A., Sidorin, A., 1992. Observations of quasi-static fault growth from acoustic emissions. In: Evans, B., Wong, T.F. (Eds.), Fault Mechanics and Transport Properties of Rocks. Academic Press, San Diego, CA, pp. 3–31.

Lundqvist, R.G., 1981. Hemispherical indentation and the design of "button bits" for percussive drilling. Proc. 22nd Symp. Rock Mech.. AIME, Cambridge, pp. 219–222.

Moore, D.E., Lockner, D.A., 1995. The role of microcracking in shear-fracture propagation in granite. J. Struct. Geol. 17 (1), 95–114.

Paterson, M.S., 1978. Experimental Rock Deformation: The Brittle Field. Springer, Berlin, p. 254.

Ramez, M.R.H., 1967. Fractures and the strength of a sandstone under triaxial compression. Int. J. Rock Mech. Min. Sci. 4, 257–268.

Shimada, M., Cho, A., 1990. Two types of brittle fracture of silicate rocks under confining pressure and their implications in the earth's crust. Tectonophysics 175, 221–235.

Tang, C.A., 1997. Numerical simulation of progressive rock failure and associated seismicity. Int. J. Rock Mech. Min. Sci. 34, 249–262.

Tang, C.A., Liu, H., Lee, P.K.K., Tsui, Y., Tham, L.G., 2000. Numerical studies of the influence of microstructure on rock failure in uniaxial compression. Part I: effects of heterogeneity. Int. J. Rock Mech. Min. Sci. 37, 555–569.

Tang, C.A., Tham, L.G., Lee, P.K.K., Yang, T.H., Li, L.C., 2002. Coupled analysis of flow, stress and damage (FSD) in rock failure. Int. J. Rock Mech. Min. Sci. 39, 477–489.

Tapponnier, P., Brace, W.F., 1976. Development of stress-induced microcracks in Westerly granite. Int. J. Rock Mech. Min. Sci. 13, 103–112.

Verhoef, P.N.W., Ockeloen, J.J., 1996. The significance of rock ductility for mechanical rock cutting. Rock Mechanics. Balkema, Rotterdam, pp. 709–716.

Wawersik, W.R., Fairhurst, C., 1970. A study of brittle rock failure in laboratory compression experiments. Int. J. Rock Mech. Min. Sci. 7, 561–575.

Weibull, W., 1951. A statistical distribution function of wide applicability. J. Appl. Mech., 293–297.

Weijermars, R., 1997. Principles of Rock Mechanics. Alboran Science Publishing, Amsterdam, The Netherlands, p. 359.

Whittaker, B.N., Singh, R.N., Sun, G., 1992. Rock Fracture Mechanics: Principles, Design and Applications. Elsevier, Amsterdam.

Wong, T.F., David, C., Zhu, W., 1997. The transition from brittle faulting to cataclastic flow in porous sandstones: mechanical deformation. J. Geophys. Res. 102, 3009–3025.

Wu, X.Y., Baud, P., Wong, T.F., 2000. Micromechanics of compressive failure and spatial evolution of anisotropic damage in Darley Dale sandstone. Int. J. Rock Mech. Min. Sci. 37, 143–160.

Zhao, J., 2000. Applicability of Mohr–Coulomb and Hoek–Brown strength criteria to the dynamic strength of brittle rock. Int. J. Rock Mech. Min. Sci. 37, 1115–1121.

Zhu, W.C., 2001. Mesoscopic numerical model for the fracture process of concrete and its application. PhD thesis, Northeastern University (in Chinese).